Journal of Marine Research, 59, 327–353, 2001

The evolution and energetics of large amplitude nonlinear internal waves on the Portuguese shelf

by D.R.G. Jeans[1,2] and T.J. Sherwin[1]

ABSTRACT

Intensive *in-situ* observations of nonlinear internal waves on the Portuguese shelf were made in August 1994, including measurements of the same wavepacket at three locations as it propagated on-shelf. The waves were characterized by sudden isotherm depressions of up to 45 m lasting 10–35 minutes, accompanied by current surges of up to 0.45 m s^{-1} and shears of up to 0.7 m s^{-1} over 60 m. The waves propagated away from the shelf break with an estimated phase speed of 0.57 m s^{-1}. The amplitude of the waves was comparable to the theoretical maximum. The kinetic and potential energies of the waves were calculated directly from the observed current and density structures. Individual waves were associated with a total energy of up to approximately 3.0 M J m^{-1} per unit crest length. The depth integrated on-shelf internal wave energy flux approached 2000 W m^{-1} per unit crest length near the shelf break and decreased on-shore at a depth integrated rate of approximately 7.7×10^{-2} W m^{-2}. The internal waves provided an important source of vertical mixing where they occurred on the Portuguese shelf throughout most of August 1994, represented by a sustained vertical eddy diffusivity profile which peaked at $K_z \approx 2.2 \times 10^{-3}$ m^2 s^{-1} at 30 m depth. Internal mixing would have to be parameterized by such a K_z profile in any model of the Portuguese shelf in which the stratification were to be accurately represented.

1. Introduction

Nonlinear Internal Waves (NIWs), sometimes called solitary internal waves, are large internal waves that are frequently found propagating away from shelf edges and sills. The dissipation of the energy contained within these waves can make an important contribution toward mixing where they occur. The large amplitude waves observed in the strongly stratified Andaman Sea by Osborne and Burch (1980) each contained up to 167 M J m^{-1} per unit crest length. On continental shelves around the world NIWs are generally less energetic, with individual waves typically containing $O(1)$ M J m^{-1} per unit crest length. For example Howell and Brown (1985) estimated 0.82 M J m^{-1} on the California Shelf, Holloway (1987) estimated 2.88 M J m^{-1} on the Australian NW Shelf and Sandstrom *et al.* (1989) estimated 3.0 M J m^{-1} on the Scotian Shelf.

1. Centre for Applied Oceanography, Marine Science Laboratories, Menai Bridge, Anglesey LL59 5EY, United Kingdom.

2. Present address: Fugro GEOS, Gemini House, Hargreaves Road, Swindon, Wiltshire SN25 5AL, United Kingdom. ***email: g.jeans@geos.com***

NIWs provide a mechanism for transporting mixing energy from their source to the deep ocean or onto the continental shelf. Brickman and Loder (1993) calculated a depth-integrated tidal mean on-shelf energy flux of 195 W m^{-1} due to the NIWs propagating onto Georges Bank each tidal cycle. This is comparable in magnitude to the cross-shelf energy fluxes of $O(100\ \mathrm{W\ m^{-1}})$ associated with the internal tide in the various regions considered by Huthnance (1989).

It is possible to estimate the average energy decay rate from an estimate of the energy flux at one location and the distance the NIWs travel before they are dissipated. For example, Sandstrom and Elliott (1984) calculated a depth-integrated decay rate of 5×10^{-2} W m^{-2} for NIWs on the Scotian Shelf and later Sandstrom *et al.* (1989) calculated a depth-integrated decay rate of 8×10^{-2} W m^{-2} for NIWs in a nearby gully.

An important mechanism of internal wave dissipation is the formation of shear instabilities in which the wave energy goes into overturning and mixing (e.g. Bogucki and Garrett, 1993). The potential for a shear flow to develop instabilities is determined by the gradient Richardson number R_i. This is the ratio between the stabilizing potential energy and the instability promoting shear energy

$$R_i = N^2(z) \Big/ \left[\left(\frac{\partial u}{\partial z} \right)^2 + \left(\frac{\partial v}{\partial z} \right)^2 \right] \tag{1}$$

where $N(z)$ is the buoyancy frequency profile and $\partial u/\partial z$ and $\partial v/\partial z$ are the vertical rates of change of the two horizontal components of velocity. A steady stratified shear flow is generally thought to become unstable to small perturbations whenever $R_i < 1/4$ (Miles, 1961). Should this condition be satisfied for long enough, instabilities will develop in the form of Kelvin-Helmholtz billows resulting in overturning and vertical mixing (Thorpe, 1973). Most of the dissipated internal wave energy goes into turbulent kinetic energy, but a significant fraction is transferred into water column potential energy by raising the center of gravity of the fluid. This fraction is referred to as the efficiency of internal mixing and is typically about 0.2 (e.g. Osborn, 1980).

Evidence for dissipation of NIWs through the development of shear instabilities has frequently been observed in the field and subcritical Richardson numbers have been observed on the Scotian Shelf (Sandstrom and Elliott, 1984) and in the Celtic Sea (New and Pingree, 1990). Temperature inversions attributed to active vertical mixing associated with NIWs have been observed by Haury *et al.* (1979) in Massachusetts Bay and by Holligan *et al.* (1985) in the central Bay of Biscay. Sandstrom *et al.* (1989) observed a shear-generated turbulent layer associated with the NIWs on the Scotian Shelf, with temperature fine structure and subcritical Richardson numbers in the thermocline. They found acoustic backscatter to be a particularly useful tool for detecting temperature fine structure. Sandstrom and Oakey (1995) later obtained direct measurements of internal mixing and estimates of turbulent kinetic energy dissipation using a microstructure profiler. They estimated a mean dissipation rate of approximately 5.3×10^{-4} W m^{-3} over a layer 10 m thick and a corresponding vertical diffusivity of $K_z = 5 \times 10^{-5}\ \mathrm{m^2\ s^{-1}}$. Inall

et al. (2000) used a dissipation probe on the Malin Shelf and found that enhanced mixing in NIWs with an elevation of about 30 m resulted in sustained dissipation rates of 1.1×10^{-2} to 4.0×10^{-2} W m^{-2} and values of K_z between 5×10^{-4} and 1.2×10^{-3} m^2 s^{-1}.

In some shelf regions the dissipation of NIWs constitutes the primary mixing mechanism. This was the conclusion of Sandstrom and Elliott (1984) for a region 20–30 km inshore of the Scotian Shelf break. Holloway (1991) found that the energy dissipated from the internal tides on the Australian North West Shelf provided all the mixing energy required to explain the observed linear temperature profile.

One important property of internal mixing is that it allows a transfer of water and its constituents between the upper and lower layers. Internal mixing due to the dissipation of the internal tide was suggested by Sherwin (1988) to be the cause of the diffuse thermocline observed on the Malin Shelf. In the Strait of Gibraltar, where NIWs are generated on the boundary between the Atlantic and Mediterranean water masses, La Violette and Arnone (1988) suggested that the strong mixing associated with the waves may significantly modify Atlantic water before it crossed the sill into the Mediterranean.

The mixing caused by the dissipation of NIWs can drive a supply of nutrients from below the thermocline into the surface layer, which can in turn boost phytoplankton growth and primary production. There have been numerous observations confirming the effect of NIW mixing on primary productivity, for example Haury *et al.* (1979) and later Haury *et al.* (1983) in Massachusetts Bay and Brickman and Loder (1993) on the northern edge of Georges Bank. Sandstrom and Elliott (1984) found that the mixing caused by the two NIWs observed per tidal cycle on the Scotian Shelf was sufficient to account for the nutrient supply required to explain the increased biological activity of the area. The presence of cool nutrient-rich surface waters extending some 50 km inshore of the Celtic Sea shelf break throughout summer was attributed to NIW mixing, rather than wind-driven upwelling, by Pingree *et al.* (1986). Holligan *et al.* (1985) provided the first evidence for enhanced surface nutrient levels caused by NIW mixing in the deep ocean environment, where vertical fluxes across the pycnocline are generally weak and phytoplankton growth in the surface waters tends to be restricted.

The Portuguese shelf is a region of high biological productivity, commonly attributed to the upwelling of relatively cold nutrient rich waters, driven by the predominantly northerly wind regime in the summer months (e.g. Fiúza *et al.,* 1982). A detailed study of NIWs on the Portuguese shelf was proposed as part of the EU MAST II MORENA (Multidisciplinary Oceanographic Research in the Eastern North Atlantic) project. The overall aims of this project were to further the understanding of, and quantify, the shelf-ocean exchange processes in the region. The specific aims of the NIW study included a detailed quantification of the NIW energy flux, decay rate and contribution toward internal mixing, and assessment of their significance compared to other processes in an upwelling region.

The next section describes the measurements of NIWs that were made on the Portuguese shelf, and is followed in Section 3 by a detailed description of the waves and their evolution across the shelf, in terms of their vertical displacements and horizontal currents. The

observations are well suited for an investigation into the way in which NIWs dissipate their energy as well as their impact on the local thermal structure. With this in mind Section 4 contains direct calculations of the energy in the waves and the rate at which it decayed across the shelf. At one station there was clear evidence of NIW mixing in the change in bulk properties of the thermocline and Section 5 quantifies the mixing from these changes. Section 6 considers the energetic relationship between the NIWs and the internal tide. Not all of the energy in the NIWs dissipates in internal mixing, and Section 7 considers other ways in which it could have been lost. Finally, the results are discussed in relation to earlier work in Section 8. The variability of the NIWs and the relationship with upwelling is discussed separately by Jeans and Sherwin (2001).

2. Method of observation

The field observations were conducted during the MORENA 3B cruise aboard the M/S *Håkon Mosby* in August 1994. An intensive internal wave observational program was carried out between 10 and 14 August, when NIWs were measured in detail at five stations on the shelf (Fig. 1). At three stations (14, 15 and 16, approximately 10 km apart) measurements were made of the same wavepacket as it propagated on-shelf.

An Aanderaa thermistor chain was deployed on a temporary mooring at each of the 5 internal wave stations. The rig was assembled with thermistors at 5 m intervals between 12 m and 37 m depth and then at 10 m intervals to 87 m depth. The relatively long response time of approximately 7 minutes, compared with the sampling interval of one minute, is due to insulation of the thermistors in the housing cable. This inevitably causes some smoothing of observed wave shapes and possibly an underestimate of wave amplitudes.

Continuous yo-yo profiles were performed using a Sea-Bird Electronics (SBE) 911 plus CTD while the ship held position approximately 100 m away from the temporary thermistor chain mooring at each internal wave station. With an ascent/descent rate of approximately 1 m s^{-1}, it took approximately 6 minutes for a complete cast to be performed in 160 m of water. The CTD profiles have a higher vertical resolution and a shorter response time compared to the thermistor chain measurements, as well as covering a larger proportion of the water column. They, therefore, provide a more detailed picture of water column structure as well as providing a measurement of salinity.

The hull-mounted RDI 150 kHz narrowband ADCP was set to record at 2.5 minute ensembles throughout the duration of the cruise. Good quality data were obtained at all stations except station 10, where the first few waves passed by while the ADCP was being repaired, and station 16, where a large proportion of bad data values were recorded. In addition to the intensive on-station measurements, three transects were made with the ship along the continental shelf and slope at about 41N, during which NIWs were resolved with the ADCP. For the purpose of examining the baroclinic velocity fields of the waves the instantaneous depth average was subtracted from every ensemble, thereby eliminating not only the ship's motion but also all barotropic motions including the tide. Throughout the

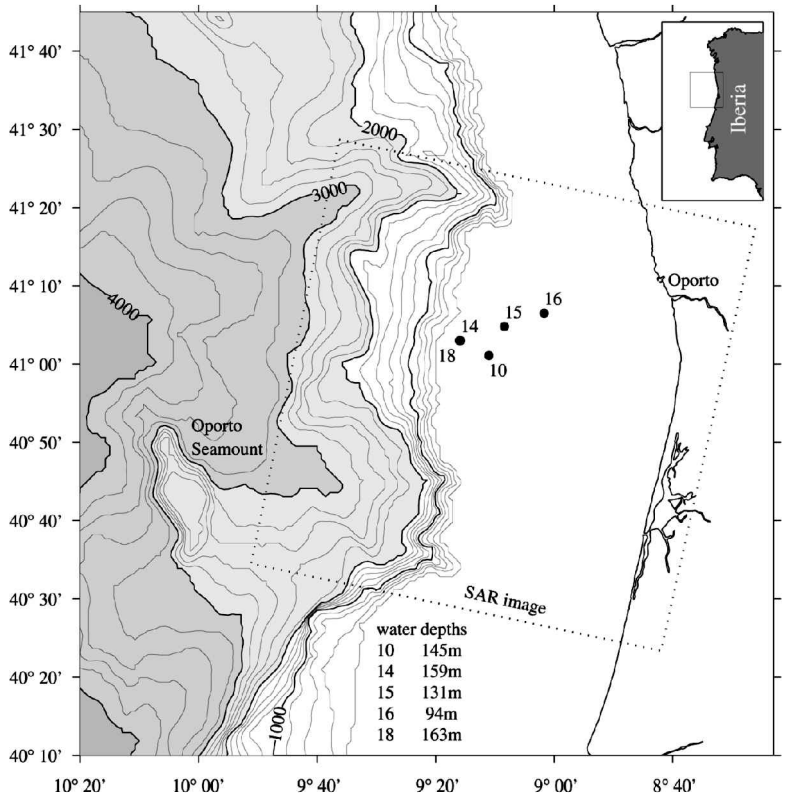

Figure 1. Bathymetry of the western Iberian margin close to 41N, showing the location of the five internal wave stations on the Portuguese shelf. The insert shows the location of the figure in relation to the Iberian peninsula. The bathymetry was supplied to the MORENA project by the Portuguese Geological Survey. The border of the SAR image in Figure 2 is shown as a dotted box.

period of measurement the remaining baroclinic signal was dominated by the internal tide and NIWs.

The surface manifestation of the NIWs was visible at several times during the cruise in the form of slicks, and was evident in a Synthetic Aperture Radar image just before the cruise began (Fig. 2). The slicks appeared to propagate on-shore in a direction perpendicular to the crests at approximately 073° T. This was assumed to be the propagation direction of the underlying NIWs and stations 14, 15 and 16 were positioned along a line of this orientation.

3. Internal wave evolution

At station 14 the observations were characterized by the sudden appearance of a train of five NIWs in the form of individual isotherm depressions (Fig. 3). The waves have been

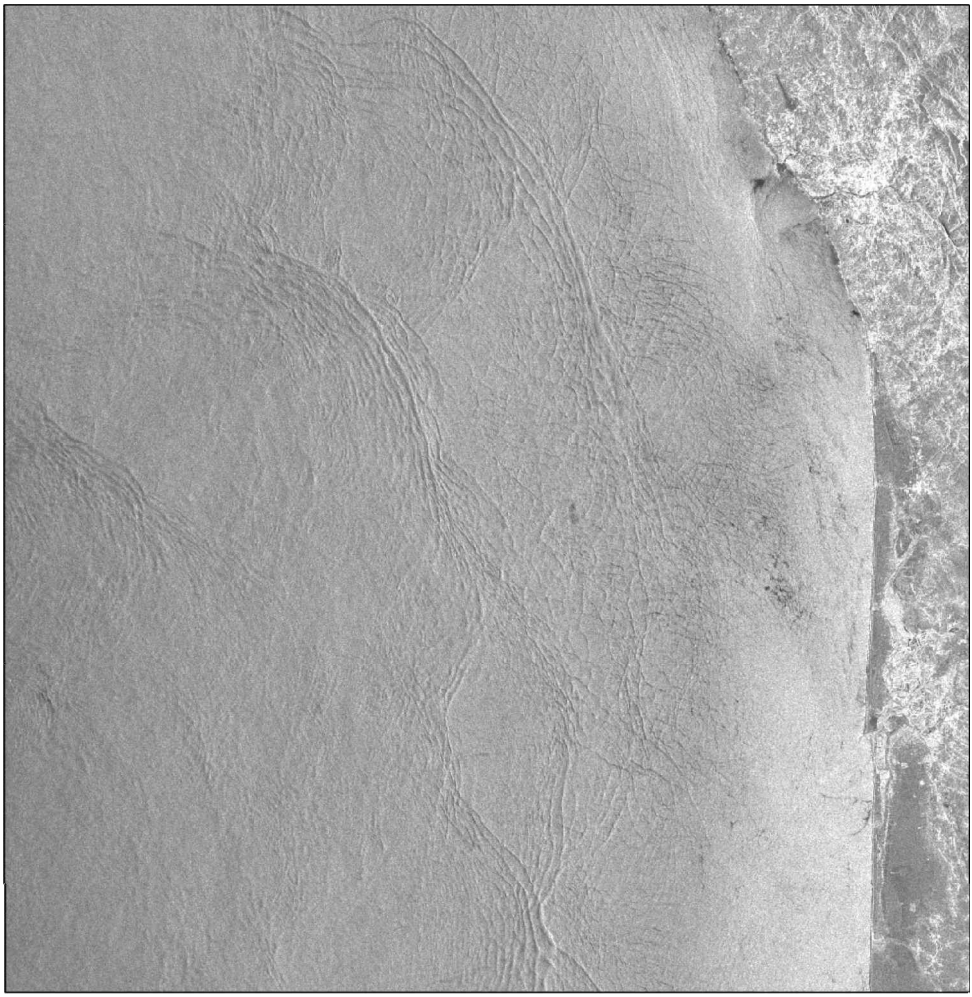

Figure 2. ERS-1 SAR image from orbit 16020, frame 2781, at 11:20 GMT 8th August 1994. Courtesy of Jose da Silva, Southampton University. Packets of NIWs can be seen propagating toward Oporto through the internal wave stations shown in Figure 1.

labelled a to e in order of appearance. The horizontal baroclinic velocities were resolved into the average direction of upper layer flow during the passage of the largest waves, which allowed the internal wave velocity field to be described with only one horizontal component. The ADCP time series has been offset by the time it took the NIWs to propagate the distance from the thermistor chain mooring to the vessel (3 minutes at station 14), so the two data sets are synchronized.

Three well-formed NIWs of approximately 35 m vertical displacement and 20 minute duration were followed by two smaller less well-formed ones. The isotherm depression of

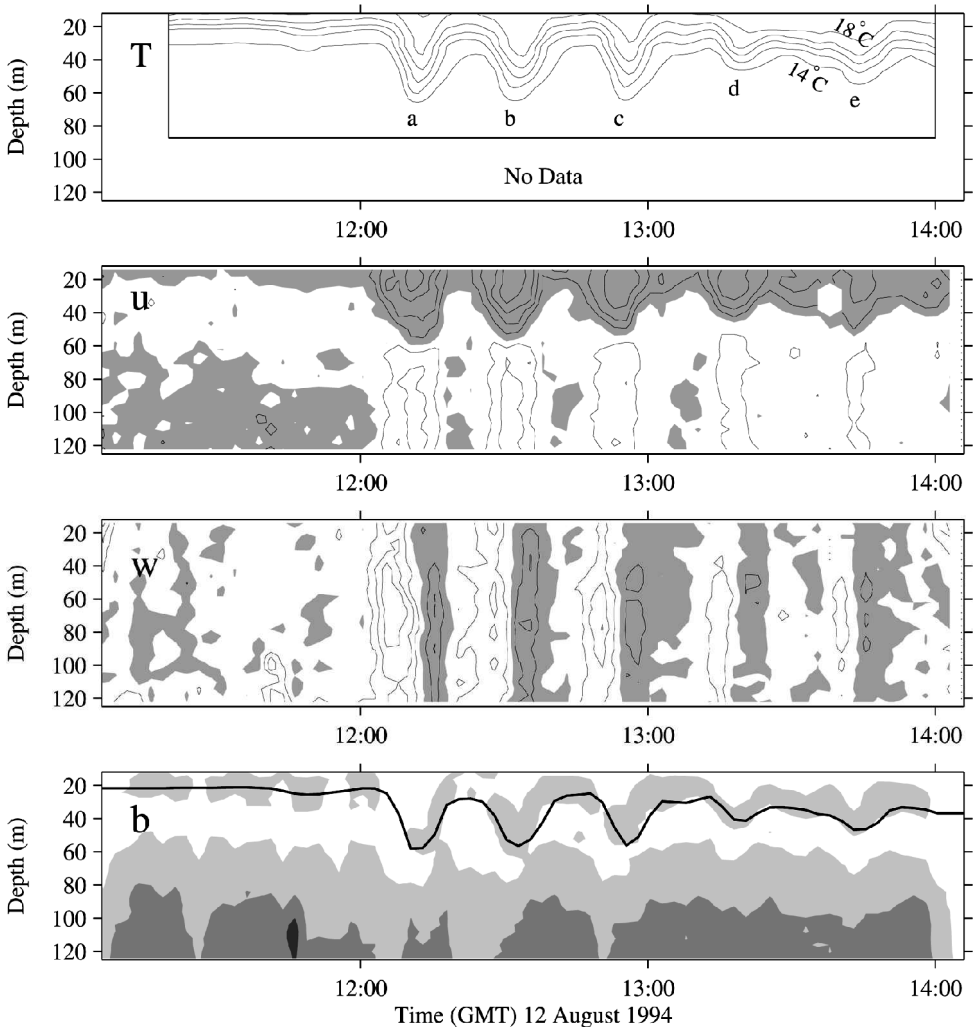

Figure 3. The wavepacket as it passed station 14. Isotherm contours (T) derived from thermistor chain measurements with the first five waves labelled a–e. Horizontal baroclinic (u) and vertical (w) velocities with contour intervals 10 cm s^{-1} and 5 cm s^{-1}, respectively and positive (toward 082°, upward) values shaded grey. Acoustic backscatter amplitude (b) with dark regions corresponding to high backscatter and the 15° isotherm overlaid.

each individual wave was accompanied by baroclinic current surges of over 0.4 m s^{-1} in the upper layer and surges of over 0.2 m s^{-1} in the opposite direction in the lower layer. The baroclinic currents were greatest in the waves that had the largest vertical displacements.

The magnitude of the baroclinic current reached a peak of nearly 0.5 m s^{-1} close to the surface during the passage of the first wave (Fig. 4). At the same time the current direction

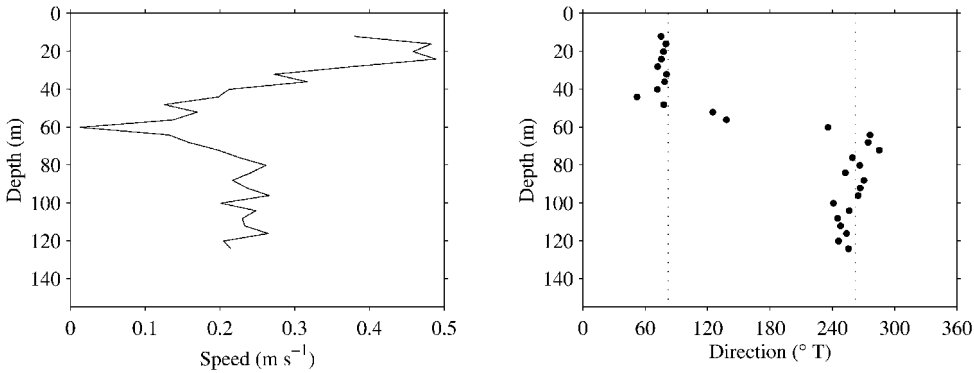

Figure 4. Profiles of horizontal baroclinic velocity magnitude and direction at 12:15 GMT during the passage of the first wave at station 14. The directions of 082° and 262° are indicated as dotted lines.

was approximately 082° throughout the upper layer, which was within 10° of the estimated propagation direction of 073°. The current direction only changed significantly across the displaced thermocline, where it rotated through almost exactly 180° and the current speed fell to nearly zero. The peak shear was approximately 0.7 m s^{-1} over a vertical distance of 60 m.

The vertical velocity field corresponded well with the isotherm displacements, with downward velocities of over 0.15 m s^{-1} as the isotherms descended on the leading edge of a wave, and upward velocities on the trailing edge. The largest velocities were associated with the largest waves.

A region of relatively high acoustic backscatter amplitude was found around the depth of the thermocline. This peak in backscatter was present before the waves arrived and appeared to be advected vertically with the thermocline as the waves passed by.

The appearance of the wavepacket had changed considerably by the time it arrived at station 15. The temperature and current field are shown in Figure 5 at the same scale as they were for station 14 to aid comparison and the ADCP time series has again been offset to synchronize it with the thermistor chain data. The first five waves are again labelled in order of appearance, but it is stressed that these labels do not necessarily correspond to the same individual waves as at station 14. The size of the vertical displacements appears not to have changed considerably overall, but the leading wave was now noticeably smaller than the following waves. Each individual wave appeared to have a shorter duration and more waves passed by in a fixed time than at station 14. The horizontal baroclinic velocities appear to have been significantly reduced.

At station 16 the waves had smaller vertical displacements and were of longer duration and farther apart than at the two previous stations (Fig. 6). Again the first five waves are labelled in order of appearance but the identification of the individual waves observed at the previous stations is virtually impossible. Currents from the ADCP were not available at this station.

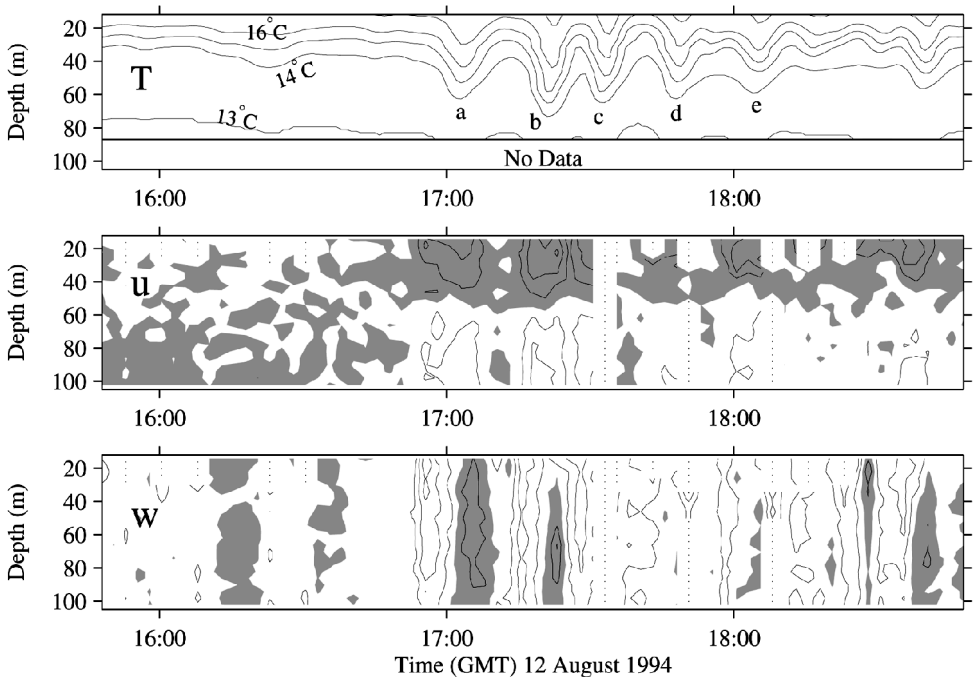

Figure 5. The wavepacket as it passed station 15. Isotherm contours (T) derived from thermistor chain measurements with the first five waves labelled a–e. Horizontal baroclinic (u) and vertical (w) velocities with contour intervals 10 cm s^{-1} and 5 cm s^{-1}, respectively and positive (toward 053°, upward) values shaded grey. Dots denote grid cells where no good data were available. The scale is the same as Figure 3.

The difference in duration of individual waves at the stations may have been due to either changes in their length or their overall propagation speed. This speed, s, can be written as $s(t) = c + u(t)$ where c is the NIW phase speed and $u(t)$ the advective tidal and residual currents. From the observations, s was 0.60 m s^{-1} between stations 14 and 15, and 0.52 m s^{-1} between stations 15 and 16. However, following subtraction of the relatively

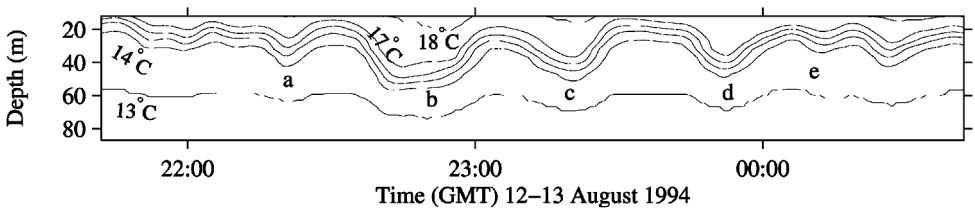

Figure 6. The wavepacket as it passed station 16. Isotherm contours derived from the thermistor chain measurements with the first five waves labelled a–e. The scale is the same as Figure 3 and Figure 5. There were no ADCP data for this station.

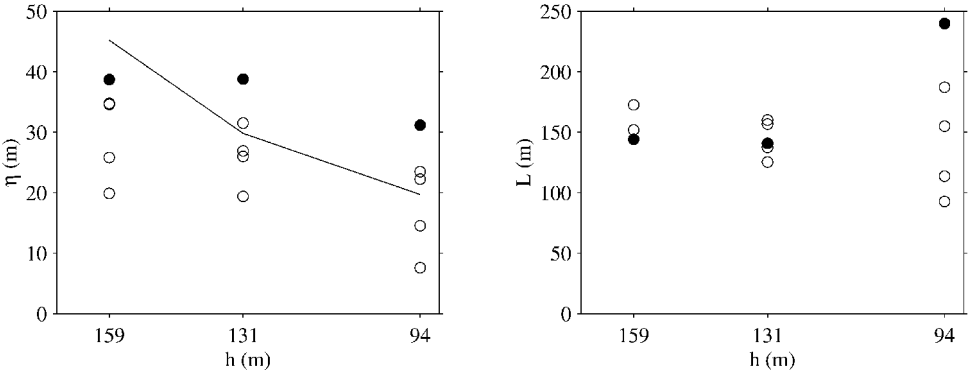

Figure 7. The amplitude (η) and length scale (L) of the five largest waves versus water depth (h) at stations 14, 15 and 16 (h = 159, 131 and 94 m, respectively). The largest amplitude wave is represented by a filled circle. The theoretical limiting wave amplitude, $\bar{\eta}$, is shown as a solid line.

small advective tidal and residual currents (derived from tidal analysis of shipboard ADCP data) the waves appear to have propagated on shore with a constant phase speed of c = 0.57 m s^{-1}. Where required, the instantaneous propagation speed of the wavepacket at any station was estimated using this constant phase speed and the predicted tidal currents.

The change in size of individual waves as they propagated into shallower water is summarized in Figure 7. The amplitude, η, is defined as the maximum vertical excursion of the 15°C isotherm from its level before the waves arrived. The horizontal length of each individual wave, L, is defined as the distance between the points on the leading and trailing edge of the wave where the 15°C isotherm was displaced by 0.42 η. This definition is consistent with analysis of NIWs elsewhere, where they have been compared with solitons (e.g. Osborne and Burch, 1980). At the two deeper stations, 14 and 15, the waves were very similar, with L clustered around 150 m and η in the range 20 to 40 m. However, by the time the wavepacket had reached station 16 the amplitudes were notably smaller and the values of L were much more spread out, ranging between 100 m and 240 m.

It is suggested that the changes that occurred at station 16 may have been due to the effects of strong nonlinearity. Strongly nonlinear internal waves have a theoretical maximum amplitude beyond which they should not grow. Following the two-layer theory of Michallet and Barthelemy (1998) and assuming that the change in density across the interface is small compared with the density in either layer, the limiting wave amplitude $\bar{\eta}$ is given by

$$\bar{\eta} = h_2 - \frac{h}{2} \tag{2}$$

where h_2 is the lower-layer thickness and h is the total water depth. It is noticeable that, in general, the waves that increased in length already had $\eta > \bar{\eta}$ at station 15 (Fig. 7). Thus, the reduction in η between stations 15 and 16 may have been due to the waves propagating

into shallower water, where $\bar{\eta}$ was smaller (Fig. 7). The increase in lengthscale is also a feature of limiting amplitude waves. These changes will be discussed further in Section 8, in relation to the energy flux and internal mixing.

4. Internal wave energy content and decay rate

The internal wave kinetic and potential energies were calculated independently from direct measurements of the velocity and density structure. This is more rigorous than the method employed by Osborne and Burch (1980) and most subsequent investigators, who have calculated the energy per unit crest length of theoretical two-layer internal solitons assuming the equipartition of kinetic and potential energy.

Energy calculations focus on the short period NIWs and exclude the internal tide, even though they may both be regarded as part of the same process. The internal tide is considered as a possible source of energy to the NIWs (Section 6). To isolate the energy of the nonlinear waves, both the kinetic and potential energy were defined as zero just before the waves arrived.

The depth-integrated internal wave kinetic energy k (per unit horizontal area) was calculated from the data according to

$$k = \tfrac{1}{2}\bar{\rho} \sum (u^2 + v^2 + w^2)\Delta z \tag{3}$$

where $\bar{\rho}$ is the mean density, u, v and w the components of baroclinic velocity, and Δz is the height of each vertical level (i.e. the ADCP bin length). The sum was performed over all ADCP bins in which good data were recorded. To isolate the contribution due to NIWs at the internal wave stations, the mean baroclinic flow, averaged over the portion of the record before the waves arrived, was subtracted from the measured baroclinic velocities before k was calculated. This operation was not performed on the ADCP data collected during the transect runs since tests showed that it actually made very little difference to the calculation of k, confirming that the baroclinic kinetic energy was dominated by NIWs.

The potential energy calculation was achieved by tracking the vertical motions of 'fluid elements' defined in terms of temperature. The gravitational restoring force $f(i, j)$ on fluid element i at time step j was calculated following Lighthill (1978) using

$$f(i, j) = g(\rho_j(z(i, j)) - \rho_0(z(i, j))) \tag{4}$$

where g is acceleration due to gravity, $\rho_j(z)$ is the density profile at time step j, $\rho_0(z)$ is the undisturbed density profile and $z(i, j)$ is the vertical elevation of the fluid element (increasing upward). It should be noted that this definition of z, used throughout the equations in this paper, is of the opposite sign to the depth shown on the figure axes. The undisturbed density profile, $\rho_0(z)$, was derived from the period just before the NIWs arrived to isolate their potential energy.

The change in potential energy is the work done against gravitational forces by the internal wave as it moves the fluid elements; i.e., the multiple of the average restoring force

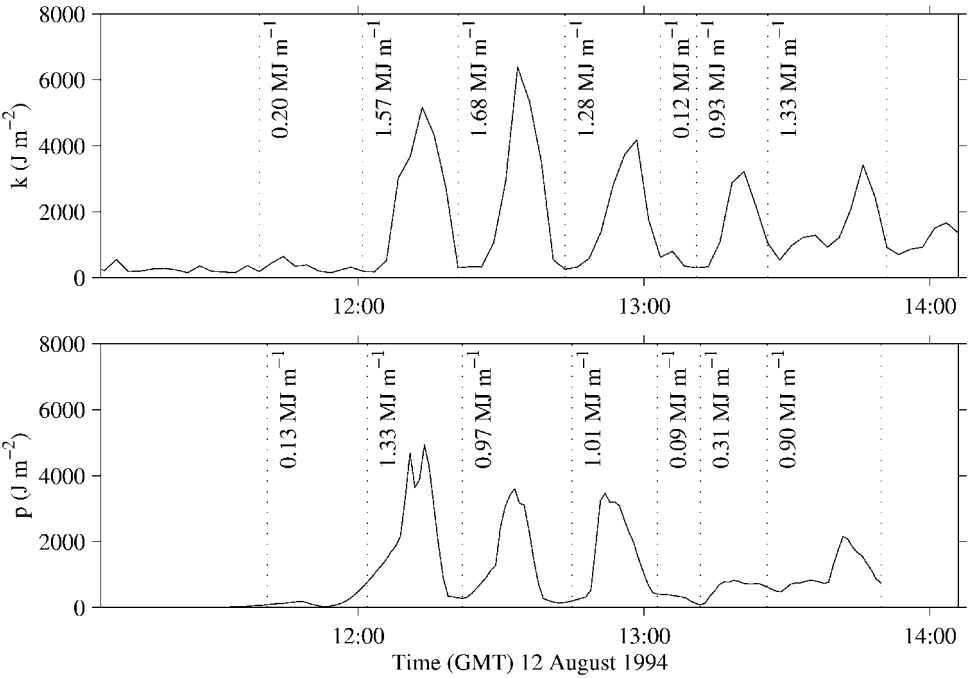

Figure 8. Time series of depth-integrated kinetic energy k and potential energy p (per unit horizontal area) at station 14. In each case the total kinetic energy K or potential energy P per unit crest length (M J m^{-1}) is given for each individual wave or portion of the record.

and the vertical distance moved. The depth-integrated internal wave potential energy (per unit horizontal area) p at time step j is given by

$$p(j) = p(j-1) + \sum_i \frac{(f(i,j) + f(i,j-1))}{2} (z(i,j) - z(i,j-1))\Delta z_{ij} \qquad (5)$$

where Δz_{ij} is the vertical extent of fluid element i at time step j. The potential energy was derived using both the CTD and the thermistor chain data. However, the CTD was preferred because it provided measurements over a larger proportion of the water column, which enabled the vertical limits in Eq. 5 to be the same as those for kinetic energy in Eq. 3.

Time series of the depth-integrated kinetic and potential energy are presented for station 14 in Figure 8. These are annotated with values of the total kinetic energy K or potential energy P per unit crest length for each individual wave or portion of the record:

$$K = s \sum_{t_2}^{t_1} k\Delta t \qquad (6)$$

$$P = s\sum_{t_2}^{t_1} p\Delta t \tag{7}$$

where the sum is performed between times t_1 and t_2, Δt is the duration between each time step and s is the wave propagation speed. In general, k (which peaked at over 6000 J m^{-2}) was higher than p (which peaked at about 5000 J m^{-2}). The kinetic energy may be slightly overestimated due to noise in the ADCP data. However, the potential energy may be slightly underestimated because the yo-yo CTD casts may have missed some of the largest vertical displacements. Given these uncertainties, the results are considered consistent with equipartition of kinetic and potential energy. The assumption of equipartition is required for estimates of the total energy to be made at those stations where the ADCP failed and for the ADCP transects.

Assuming there was no source of energy to, or loss of energy from the waves, the depth integrated on-shelf energy flux would be conserved as they propagate onto the shelf. The average depth integrated flux, F, associated with a wavepacket is given by

$$F = \frac{c_g \Delta t}{(t_2 - t_1)} \sum_{t_2}^{t_1} (k + p) \tag{8}$$

where c_g is the group velocity (which for the high frequency long waves is equal to the phase speed $c = 0.57$ m s^{-1}). Values of F were calculated for each internal wave station and for ADCP transects T2 and T3 (Fig. 9). In each case t_1 and t_2 in Eq. 8 were selected so that the average was calculated over the first five waves. Equipartition of kinetic and potential energy was assumed for stations 10 and 16 and the ADCP transects where either density or velocity data were unavailable. This assumption may lead to small inconsistencies if either the potential energy was underestimated or the kinetic energy was overestimated.

Assuming the energy contained within the first five waves represents the total amount that was transferred onto the shelf due to NIWs in a tidal cycle, then the average flux over a semidiurnal tidal cycle F_{M2} is

$$F_{M2} = \frac{F(t_2 - t_1)}{T_{M2}} \tag{9}$$

where $(t_2 - t_1)$ is the duration of the wavepacket (used in Eq. 8) and $T_{M2} = 12.42$ hours is the period of the M2 tide. The most intense waves in each wavepacket generally passed by within about 2 hours, so the tidal average on-shelf energy flux is about one sixth of the flux averaged over the first five waves. For example $F = 1835$ W m^{-1} and $F_{M2} = 268$ W m^{-1} at station 14.

The energy flux clearly decreased as the waves propagated on-shelf (Fig. 9). The rate at which the energy was lost from the wavepacket that was observed at three positions on the

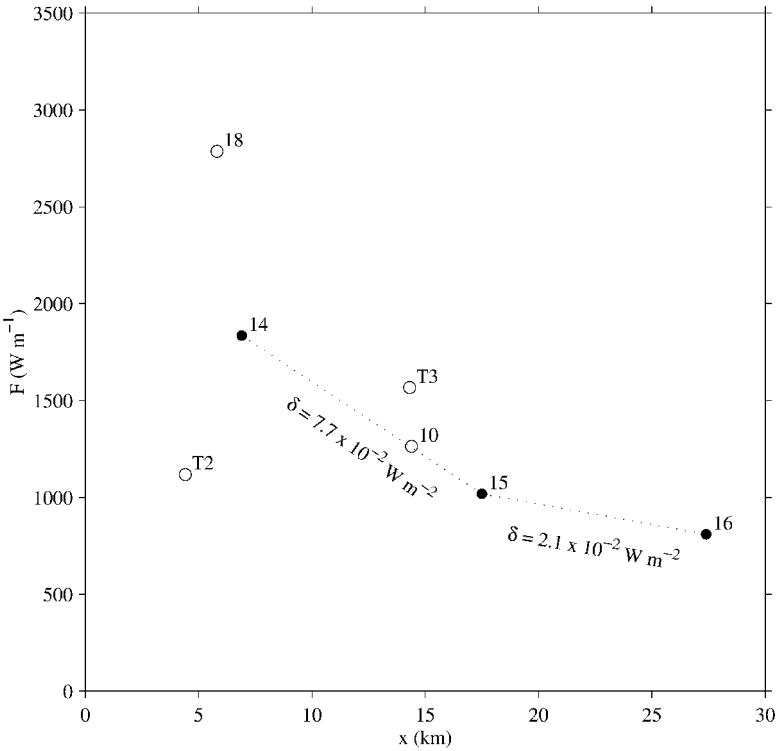

Figure 9. Depth integrated on-shelf energy flux F over the first five waves versus distance from the 200 m isobath along 073° T. The depth integrated decay rates δ between stations 14, 15 and 16 are indicated.

shelf was estimated directly from the reduction in energy flux ΔF between each station. This depth-integrated decay rate δ is given by

$$\delta = \frac{\Delta F}{\Delta x} \tag{10}$$

where Δx is the distance between each station along the direction of wave propagation. The average depth-integrated decay rate was $\delta = 7.7 \times 10^{-2}$ W m^{-2} as the waves travelled between stations 14 and 15, but only $\delta = 2.1 \times 10^{-2}$ W m^{-2} between stations 15 and 16. This change in the decay rate will be discussed in relation to wave evolution and internal mixing in Section 8.

It should be noted that if the potential energy were underestimated, then the decay rate between stations 15 and 16 would be an overestimate because the total energy at station 16 was derived from potential energy alone assuming equipartition. However, considering the comparatively small decay rate between stations 15 and 16, a significant overestimate is considered unlikely.

5. Vertical mixing

It is to be expected that a significant proportion of the energy that was lost by the NIWs as they propagated on shore was transformed into the potential energy of the water column. To quantify the energy input to the water column, changes in its structure were examined in detail at station 18, where measurements were made at the same location for several hours both before and after the wavepacket passed by.

Before the waves arrived at station 18 there was a sharp kink in both the temperature and density profiles (Fig. 10a). The rapid changes in isotherm depth during the passage of an individual wave were demonstrated by dramatic differences between consecutive CTD upcast and downcasts (Fig. 10b). There was evidence for fine structure in the temperature, salinity and density profiles and dynamically unstable inversions suggest the presence of an overturning event between 40 m and 60 m depth. The ship was held on station throughout the duration of the yo-yo CTD casts, and since the relative motion between the CTD and the waves was too small to cause the observed temperature inversions they must have been real features of the water column.

The sharp kink in the profiles before the waves arrived was eroded during their passage and the pycnocline was considerably more diffuse after they had passed by (Fig. 10c). This suggested that the waves imparted some of their energy to the water column by promoting internal mixing.

In order to investigate evidence for internal mixing from the CTD and ADCP observations, the local gradient Richardson numbers (Eq. 1) were calculated over a vertical interval of 4 m (the ADCP bin size). Since the vertical scale of the waves was much larger than 4 m it is reasonable to expect to find values of Ri that were less than 0.25. Subcritical values of Ri were found in the region of the displaced thermocline during the passage of NIWs at both stations 14 and 18 (Fig. 11), which were at approximately the same position on the shelf. Individual waves were more clearly defined at station 14, where the correlation with low Ri is more striking. Evidence for vertical mixing in CTD profiles made after the passage of the waves at station 18 should be found around the thermocline, which was advected back toward the surface after the waves had passed by, rather than in the part of the water column where the mixing would have originally occurred.

The changes in the density profiles were assumed to be primarily caused by vertical mixing and vertical advection by the internal tide. Unfortunately, there are no simultaneous temperature measurements at other locations to enable an examination of the contribution from horizontal advection in the upper water column. However, the assumption that this contribution was small is supported by the negligible change in temperature in the upper 10 m of the water column. This is where one might expect to find a significant effect, since it is where and advective currents associated with baroclinic processes would have been comparatively large.

The effect of vertical advection must be removed before vertical mixing can be

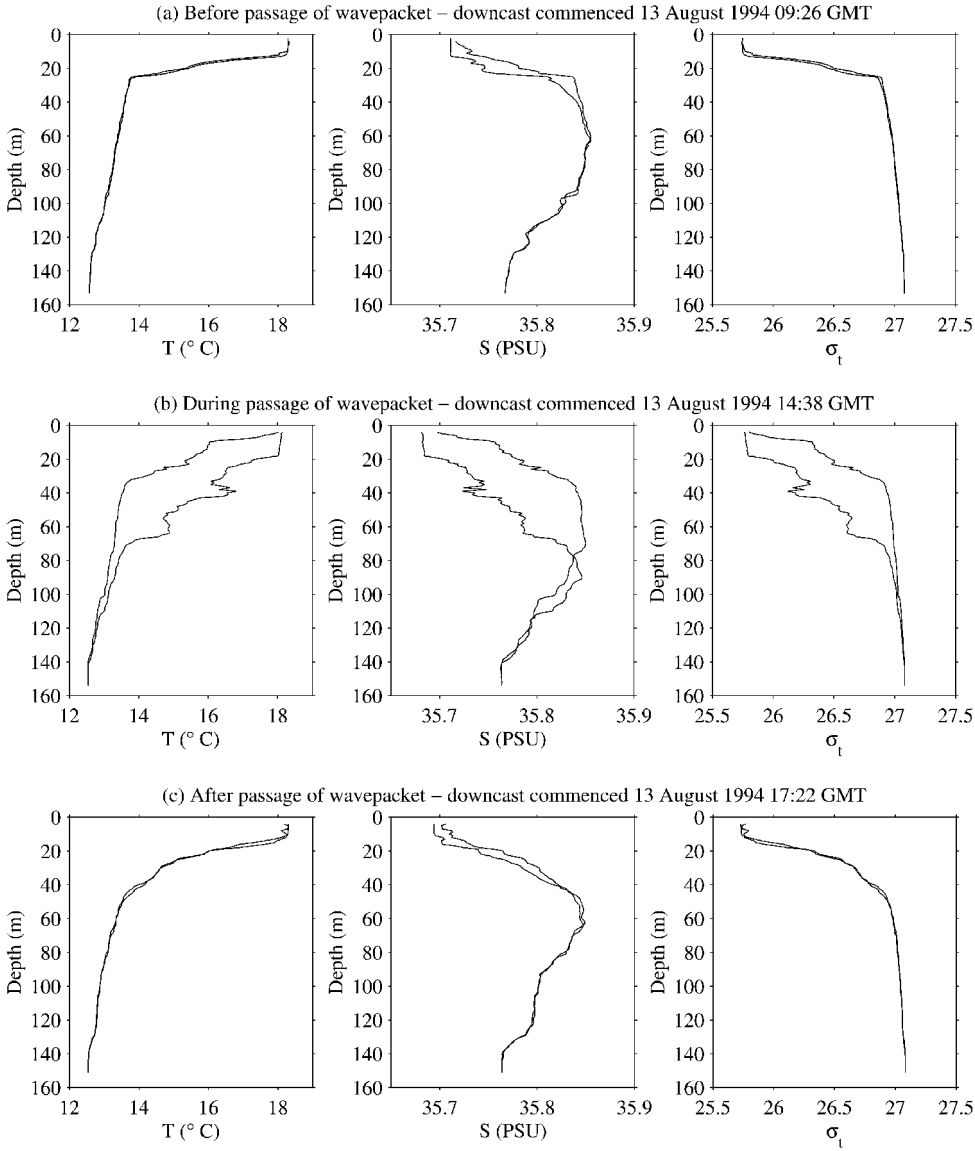

Figure 10. Temperature, salinity and density profiles made (a) before, (b) during and (c) after the passage of the wavepacket observed at station 18. Both upcasts and downcasts are shown. The figures show (a) the sharp interface before the passage of the NIWs, (b) obvious overturning event during the passage of the largest wave and (c) a diffuse thermocline after the waves had passed by.

quantified. To account for vertical advection by the internal tide, the final profile was distorted vertically with a mode one vertical velocity profile $w_1(z)$ derived from the solution of (e.g. Apel, 1987)

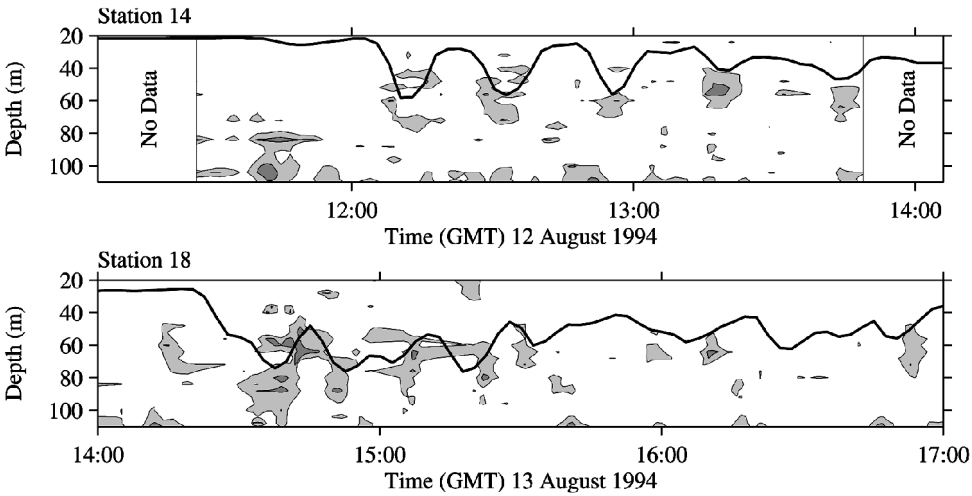

Figure 11. The gradient Richardson number Ri derived from CTD and ADCP data at stations 14 and 18. Contours are shown at $Ri = 1.00$ and $Ri = 0.25$. The heavy line shows the depth of the isotherm that underwent the largest depression (15°C at station 14 and 14°C at station 18).

$$\frac{\partial^2 w_i(z)}{\partial z^2} + \frac{\sigma^2}{c_i^2}\left(\frac{N^2(z) - \sigma^2}{\sigma^2 - f^2}\right) w_i(z) = 0 \tag{11}$$

where $w_i(z)$ and c_i are the nondimensional vertical velocity profile and associated phase speed for each mode i of the internal tide; σ is the tidal frequency; f is the inertial frequency and $N(z)$ is the buoyancy frequency profile. Eq. 11 was solved for a particular $N(z)$ profile with the boundary conditions $w_i = 0$ at the water surface and the seabed. Measurements were not conducted at station 18 for long enough to derive an average $N(z)$ profile over a complete tidal cycle. Instead it was calculated from the mean of the initial and final density profiles, which approximate the highest and lowest levels of isotherm fluctuation due to the semidiurnal period internal tide.

The solution of Eq. 11 yields $w_i(z)$ and c_i for each mode i, with higher modes having increasingly complicated vertical structures. Both the CTD and ADCP observations strongly suggested that only first mode vertical advection was significant, and this proved sufficient for the characteristic signature of internal mixing to be revealed (Fig. 12). In order to determine the absolute velocity profile with which to distort the final density profile, w_1 was scaled by a factor α which had to be determined empirically.

Although the mean density over the part of the water column in which vertical mixing occurs can be changed by vertical advection, it should be unchanged by vertical mixing. Consequently, α was determined by requiring that the mean density of the distorted final profile be the same as that of the initial profile between two fixed depths.

The initial and distorted final temperature profiles cross one another at several depths (Fig. 12) but only one crossing point is expected due to internal mixing. So α was

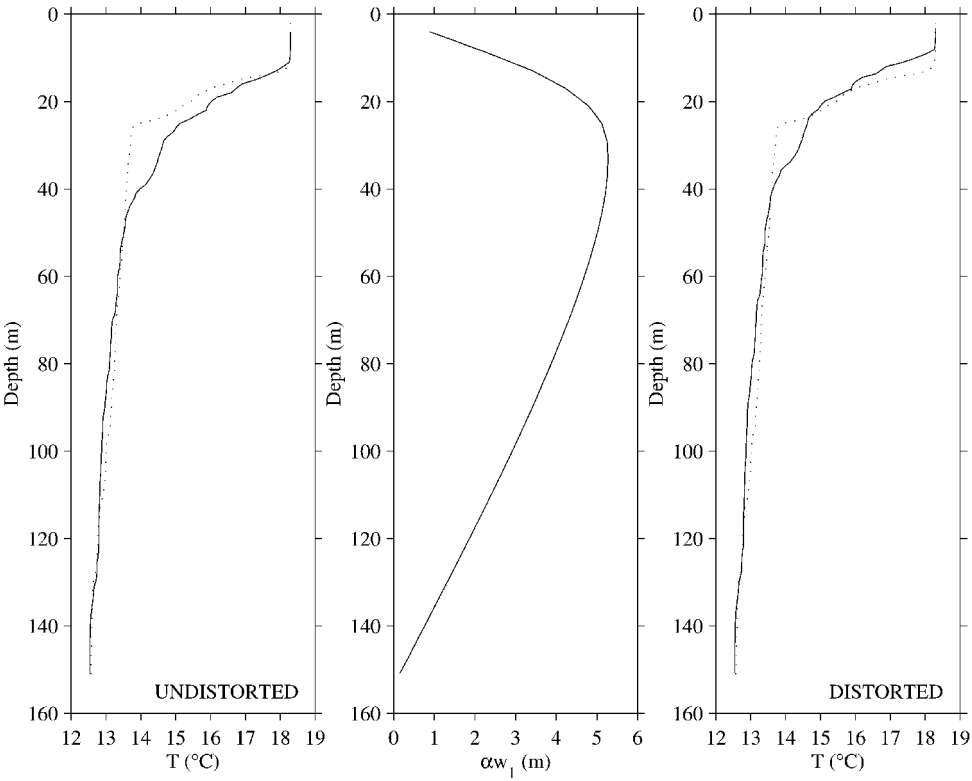

Figure 12. Comparison of the initial (broken line) and final (solid line) temperature profiles at station 18, showing both the undistorted (left) and the distorted (right) profiles. The scaled mode one vertical displacement (αw_1) used to distort the final profile is shown in the center.

determined using mean densities calculated between 7 m and 41 m, encompassing the observed mixing across the thermocline. Small differences between the initial and final profiles below 41 m were not characteristic of internal mixing and were presumably due to horizontal advection.

With the optimum value of α, the vertical offset reached a maximum of approximately 5 m at the peak in the w_1 profile. This is consistent with the amplitude of the linear internal tide observed on the Portuguese shelf in August 1994 (Jeans and Sherwin, 2001).

Having removed vertical advection, the change in depth integrated water column potential energy $\Delta\phi$ due to internal mixing can be quantified by

$$\Delta\phi = \sum_z (\rho_F(z) - \rho_0(z)) g z \Delta z \tag{12}$$

where $\rho_0(z)$ and $\rho_F(z)$ are the initial and final density profiles (Fig. 12), g is the acceleration due to gravity, z is vertical elevation (increasing upward) and Δz is the extent of each vertical level over which the sum is performed.

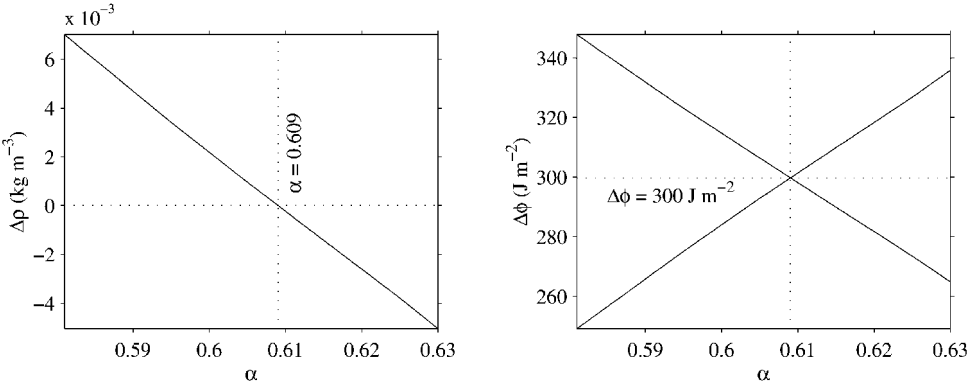

Figure 13. The change in depth mean density $\Delta\rho$ and the change in water column potential energy $\Delta\phi$ versus the vertical advection parameter α. The separate calculations of $\Delta\phi$ with $z = 0$ at the water surface and $z = 0$ at the sea bed are shown as separate lines, which converge when α is optimized such that $\Delta\rho = 0$. The values of α and $\Delta\phi$ at optimisation are given.

The calculation of $\Delta\phi$ should be independent of the choice of the $z = 0$ reference level and to test this the calculation was performed twice; with $z = 0$ at the sea bed and with $z = 0$ at the sea surface. This provided a valuable method of determining how accurately α needed to be determined, because the two calculations of $\Delta\phi$ gave dramatically different results if the mean density over the selected portion of the water column was only slightly different. For example, a density difference of 1.0×10^{-2} kg m^{-3} caused a difference of almost 50% in the values of $\Delta\phi$ (Fig. 13). The two values of $\Delta\phi$ converged as the density was conserved.

The increase in depth-integrated water column potential energy associated with the passage of the waves was estimated to be $\Delta\phi = 300$ J m^{-2} (Fig. 13). This corresponds to an average depth-integrated rate of work against buoyancy forces of $\partial\phi/\partial t = 1.0 \times 10^{-2}$ W m^{-2} over the 8 hour period between the CTD casts. Assuming that this rate is representative of the total amount of energy imparted to the water column over a whole tidal cycle, and that similar waves occurred every tidal cycle, the sustained rate of work is $\partial\phi/\partial t = 6.9 \times 10^{-3}$ W m^{-2}. However, if most of the work was actually done during the two hour period when the largest waves passed by, then a reasonable upper bound for the instantaneous rate of work against buoyancy forces becomes $\partial\phi/\partial t = 4.2 \times 10^{-2}$ W m^{-2}.

The initial and distorted temperature profiles were also used to estimate the effective vertical eddy diffusivity K_z induced by the waves. The rate of change of temperature $\partial T/\partial t$ can be expressed in terms of the vertical temperature gradient $\partial T/\partial z$ as

$$\frac{\partial T}{\partial t} = \frac{\partial}{\partial z} K_z \frac{\partial T}{\partial z}. \tag{13}$$

Eq. 13 was rewritten in space-centered finite difference form, with levels every 1 m and solved for K_z by matrix inversion. Appropriate boundary conditions were applied, where

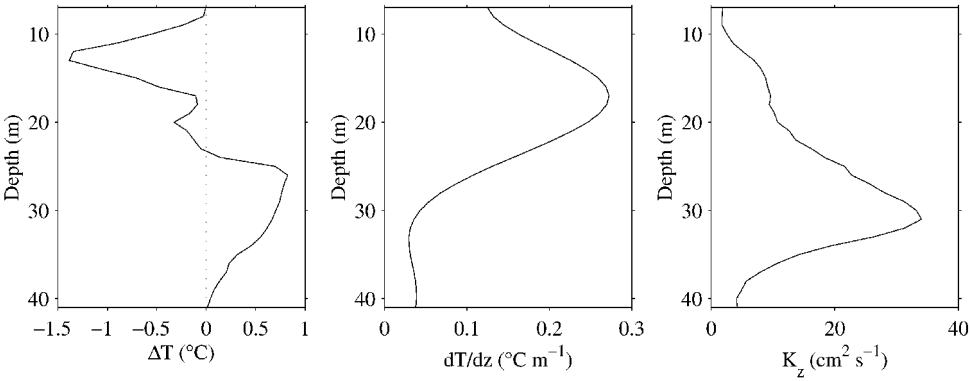

Figure 14. Stages in the calculation of the vertical eddy diffusivity K_z. On the left is the profile of the change in temperature ΔT between the initial and distorted final profiles, in the centre is the profile of the smoothed vertical temperature gradient dT/dz and on the right is the calculated K_z profile.

K_z was assumed to become independent of depth at the upper and lower boundaries. The temperature profiles were also smoothed to obtain well behaved derivatives.

The resulting K_z profile had a peak value of approximately 3.4×10^{-3} m^2 s^{-1} situated at about 30 m depth (Fig. 14). The mean value over the 34 m mixing layer was 1.4×10^{-3} m^2 s^{-1}. It is important to note that K_z represents the mean vertical mixing rate over the 8 hour observation period, and not the intensified mixing within the waves themselves. The values of K_z could have been up to 1.4×10^{-2} m^2 s^{-1} if the mixing were concentrated within the 2 hour duration of the largest waves, while the sustained value over a tidal period would have been lower, with a peak value of about 2.2×10^{-3} m^2 s^{-1}.

6. Energy from the internal tide

The internal tide was apparently responsible for a 5 m depression of the isotherms as the wavepacket passed station 18 (Section 5). This depression provides a potential source of energy to the shorter NIWs. Henyey and Hoering (1997) considered the energetics of NIWs in the presence of such a change in the upper layer thickness, using the term 'solibore' to describe this mixed soliton and borelike waveform. They derived the following expression for the rate of supply of energy per unit crest length $\partial E/\partial t$ in a two-layer irrotational system

$$\frac{\partial E}{\partial t} = -\frac{1}{2}\bar{\rho}c^3\frac{(h_f - h_i)^2}{h_f^2(h - h_f)^2}[h^2 h_i + h h_f(h_f - 2h_i)] + \frac{1}{2}g\Delta\rho c(h_f - h_i)^2 \qquad (14)$$

where c is the internal wave phase speed, h_i and h_f are the initial and final values of the upper layer thickness respectively, h is total water depth and $\Delta\rho$ is the density difference between the upper and lower layers. The depth-integrated rate of supply of energy ξ becomes

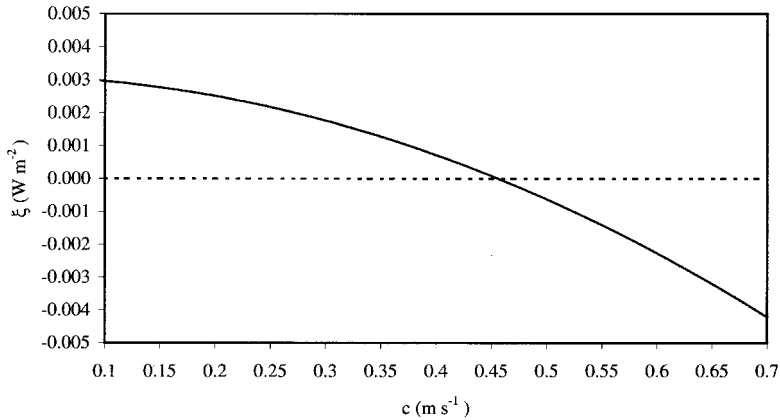

Figure 15. The depth integrated rate of supply of energy ξ from solibore theory as a function of phase speed c at station 18.

$$\xi = c\Delta t \frac{\partial E}{\partial t} \tag{15}$$

where Δt is the 8-hour interval between the initial and final CTD casts over which the 5 m depression ($h_f - h_i$) occurred. The solibore theory suggests that the internal tide could be a loss of energy for phase speeds greater than 0.45 m s^{-1}, and a source of energy at slower speeds (Fig. 15). At the observed phase speed $c = 0.57$ m s^{-1}, $\xi = -1.8 \times 10^{-3}$ W m^{-2}. This is more than an order of magnitude smaller than the decay rate estimated in Section 4 and consequently should not make a significant contribution to the overall energy budget.

The theoretical linear phase speed of the mode one internal tide was $c_1 = 0.56$ m s^{-1} from Eq. 11, which is almost identical to the observed phase speed of the NIWs. However, the phase speeds of NIWs and the internal tide are enhanced over the linear phase speed by completely different physical processes (nonlinearity and rotation, respectively), so it is not immediately apparent why they should be so similar. The phase speed dependence of solibore theory may provide an important physical insight into this problem.

The solibore term removes energy from waves traveling faster than a critical speed and feeds it into waves propagating more slowly. Presumably, energy removed from a fast-moving wave will slow it down, whilst energy fed into a slow-moving one will speed it up. If this is the case, then the solibore term should be self regulating and always tend toward zero, possibly exerting a control on the wave phase speed.

The fact that the critical speed at which the solibore term became zero was less than the observed and internal tide phase speeds may be because Eq. 14 omits dispersion due to the Earth's rotation.

7. The energy budget

The depth-integrated decay rate of the wavepacket as it propagated between stations 14 and 15 was estimated to be $\delta = 7.7 \times 10^{-2}$ W m^{-2} in Section 4, but before this value can be related to the rate of work against buoyancy forces (Section 5) the other terms in the energy budget equation must be determined. Assuming the energy input from the internal tide is zero (Section 6) the balance is

$$\delta = \varepsilon_I + \varepsilon_B + r \tag{16}$$

where ε_I represents the rate of energy loss due to internal mixing, ε_B the dissipation due to bottom boundary layer friction and r the loss due to radial spreading.

An estimate of bottom boundary layer dissipation is given by (e.g. Simpson *et al.,* 1996)

$$\varepsilon_B = \bar{\rho} d_B u^3 \tag{17}$$

where the drag coefficient is $d_B = 2.5 \times 10^{-3}$ and u is the current speed close to the bed. An upper bound estimate of $\varepsilon_B = 2.1 \times 10^{-2}$ W m^{-2} is obtained by taking $u = 0.2$ m s^{-1}.

The average loss of energy to radial spreading as a wavepacket propagates a distance Δx between two stations is given by

$$r = \frac{F}{\Delta x}\left[1 - \frac{R}{R + \Delta x}\right] \tag{18}$$

where R is the initial radius of curvature of the wave crests. The SAR image (Fig. 2) suggests a minimum radius of curvature of approximately $R = 100$ km which gives an upper bound of $r = 1.8 \times 10^{-2}$ W m^{-2} between stations 14 and 15, using values for F and Δx in Figure 9.

Using the upper bound estimates for the other terms on the right-hand side of Eq. 16, a lower bound on the rate of energy loss due to internal mixing is $\varepsilon_I = 3.8 \times 10^{-2}$ W m^{-2}. A lower bound on the mean rate of work against buoyancy forces for the wavepacket between stations 14 and 15 can be estimated from

$$\frac{\partial \phi}{\partial t} = e_I \varepsilon_I. \tag{19}$$

Assuming an internal mixing efficiency of $e_I = 0.2$ (e.g. Osborn, 1980) we get $\partial\phi/\partial t = 7.6 \times 10^{-3}$ W m^{-2} (Table 1). This is comparable to the sustained rate of work of $\partial\phi/\partial t = 6.9 \times 10^{-3}$ W m^{-2} estimated from the changes in water column structure at station 18 and an order of magnitude smaller than the upper bound for the instantaneous rate of work of $\partial\phi/\partial t = 4.2 \times 10^{-2}$ W m^{-2}. A higher decay rate can be expected at station 18, where the energy flux was greater than at station 14 (Fig. 9).

Table 1. Summary of depth-integrated terms in the energy budget equation for the wavepacket as it propagated between stations 14 and 15

δ* ($\times 10^{-2}$ W m^{-2})	ε_B† ($\times 10^{-2}$ W m^{-2})	r‡ ($\times 10^{-2}$ W m^{-2})	ε_I§ ($\times 10^{-2}$ W m^{-2})	$\partial\phi/\partial t$** ($\times 10^{-2}$ W m^{-2})
7.7	2.1	1.8	3.8	0.8

*Average decay rate
†Upper bound rate of energy loss to bottom boundary layer dissipation
‡Upper bound rate of energy loss to radial spreading
§Lower bound rate of energy loss to internal mixing
**Lower bound rate of input to water column potential energy due to internal mixing

8. Discussion

The measurement of the same wavepacket at three locations as it propagated on-shelf has allowed a detailed quantification of the energy content and decay rate of NIWs on the shelf. The dataset would be suitable for validation of internal wave evolution models that include the effects of dissipation, shoaling and strong nonlinearity.

The depth integrated on-shelf energy flux due to the NIWs was over 1800 W m^{-1} close to the shelf break. Compared to the observations discussed in the introduction, the tidally averaged values (approximately 270 W m^{-1}) were larger than NIWs on Georges Bank (Brickman and Loder, 1993) and comparable to the values associated with the internal tide considered by Huthnance (1989). The energy content of an individual wave (up to approximately 3 M J m^{-1}) is similar to values on Georges Bank, the Scotian Shelf (Sandstrom *et al.,* 1989) and the Australian NW Shelf (Holloway, 1987). The depth-integrated decay rate of $\delta = 7.7 \times 10^{-2}$ W m^{-2} is similar to the values reported by Sandstrom and Elliott (1984) and Sandstrom *et al.* (1989) on the Scotian Shelf.

The decay rate between stations 14 and 15 was notably greater than that between stations 15 and 16 (Fig. 9), even though the change in amplitude of the waves suggests that perhaps the opposite should have been the case (Fig. 7). However, the large increase in horizontal length that accompanied the reduction in amplitude between stations 15 and 16 is consistent with the relatively minor overall change in the energy flux. The decay rate was probably higher before station 15 because the waves were more energetic there, with stronger current speeds that would make them more prone to dissipation via bottom stress and internal mixing.

The change in the structure of the water column due to internal mixing during the passage of a wavepacket has been observed and quantified. The waves at station 18 were responsible for an increase in water column potential energy and the internal mixing may be parameterized by a sustained vertical eddy diffusivity profile, which peaked at approximately $K_z = 2.2 \times 10^{-3}$ m^2 s^{-1} at 30 m.

The values of K_z due to NIW mixing are an order of magnitude greater than typical values in high shear regions of the deep ocean (e.g. Osborn, 1980). However, they are also

orders of magnitude smaller than values due to tidal stirring in shelf seas with comparatively strong tidal currents (e.g. Simpson *et al.,* 1996).

The sustained K_z profile could be used to represent NIW internal mixing in numerical models that do not resolve changes within a semidiurnal tidal cycle. A higher value, active for a shorter duration within each tidal cycle, would be more appropriate for models with a finer temporal resolution that were capable of resolving more rapid changes in water column structure. The high vertical diffusivity in the thermocline means that vertical mixing would be critically underestimated on the Portuguese shelf in summer using a traditional turbulence closure scheme.

Estimates of vertical diffusion in NIWs that have been derived from direct measurements of small-scale dissipation range from $K_z = 5 \times 10^{-5}$ m^2 s^{-1} on the Scotian Shelf (Sandstrom and Oakey, 1995) to between 5.0×10^{-4} and 1.2×10^{-3} m^2 s^{-1} on the Malin Shelf (Inall *et al.,* 2000). The values on the Portuguese Shelf are marginally greater than on the Malin Shelf and much greater than on the Scotian Shelf, which is consistent with the observation of larger amplitude waves.

Nevertheless, some doubts remain about how accurately $\partial\phi/\partial t$ and K_z can be estimated from changes in the water column structure. It is possible that some of the changes that are attributed to internal mixing were really due to horizontal or vertical advection. However, the signature of internal mixing was particularly striking at station 18 and every effort has been made to quantify K_z reliably from the available data. The correction for vertical advection by the mode one internal tide provided a practical method for isolating the signature of internal mixing in the appropriate part of the water column and gave a realistic value for K_z. Critically, the mean density was conserved over that part of the water column, while the temperature at the upper and lower boundaries remained unchanged. The validity of the approach is confirmed by consistency with the independent estimate of $\partial\phi/\partial t$ for the wavepacket that propagated between stations 14 and 15 (Section 7). The values of $\partial\phi/\partial t$ and K_z derived from station 18 should be considered reliable to better than an order of magnitude. The observation thus exists as a striking example of the direct effect that a packet of NIWs can have on the structure of the seasonal thermocline.

The estimated upper bound on the rate of NIW energy loss due to bottom boundary layer dissipation ($\varepsilon_B = 2.1 \times 10^{-2}$ W m^{-2}) was comparable to the lower bound on the rate of energy loss due to internal mixing ($\varepsilon_I = 3.8 \times 10^{-2}$ W m^{-2}), but is generally understood to be far less efficient. For example Simpson and Bowers (1984) quote a mixing efficiency of 0.37%, two orders of magnitude smaller than the estimated internal mixing efficiency. With these values, the input to the water column potential energy due to bottom boundary layer dissipation was insignificant compared with the input attributed to internal mixing.

NIW mixing is considerably more significant than bottom boundary layer mixing due to the weak semidiurnal barotropic tides on the narrow Portuguese shelf, which can be represented by a depth-integrated current of approximately $Q = 10$ m^2 s^{-1} (Jeans and Sherwin, 2001). The peak tidal currents between stations 14 and 15 would be responsible for dissipation at a rate of just $\varepsilon_B = 8.4 \times 10^{-4}$ W m^{-2} (Eq. 17) which would have a

negligible effect on the water column potential energy compared to internal mixing. A similar result was found for the internal tide on the Malin Shelf by Sherwin (1988).

Wind mixing is only one order of magnitude less efficient than internal mixing and supplies energy to the water column at a rate given by (following Simpson and Bowers, 1984)

$$\frac{\partial \phi}{\partial t} = e_W d_S \rho_a s_W^3 \tag{20}$$

where $e_w = 0.023$ is the efficiency of wind mixing, $d_S = 6.4 \times 10^{-5}$ is the surface drag coefficient multiplied by the slippage factor, $\rho_a = 1.3$ kg m^{-3} is the density of air and s_W is the wind speed. The scalar mean wind speed for August 1994 was 6.1 m s^{-1} (at 41 N 9.66 W from the UK Meteorological Office Cray European model) for which the power input to the water column is $\partial\phi/\partial t = 4.3 \times 10^{-4}$ W m^{-2}. This is an order of magnitude smaller than the sustained rate of work against buoyancy forces of $\partial\phi/\partial t = 6.9 \times 10^{-3}$ W m^{-2} attributed to internal mixing at station 18. The maximum wind speed in August 1994 of 14.4 m s^{-1} was responsible for a power input of $\partial\phi/\partial t = 5.4 \times 10^{-3}$ W m^{-2}. This value is comparable to the sustained rate of work due to NIW internal mixing, but is an order of magnitude smaller than the upper bound for the instantaneous rate of $\partial\phi/\partial t = 4.2 \times 10^{-2}$ W m^{-2}. It would appear that wind mixing was less significant than NIW mixing on the Portuguese shelf for most of August 1994.

It is important to distinguish between the nature of internal and boundary mixing at the sea bed and the sea surface. While boundary mixing tends to be inhibited in the thermocline, it is precisely in this region that internal mixing is greatest. Internal mixing is, therefore, likely to have far greater consequences for the exchange of properties across the thermocline, such as the transfer of nutrients into the illuminated upper layer, critical to primary production. The breakdown of stratification at station 18 illustrates this point very vividly.

The Atlantic Iberian margin is a classic eastern boundary upwelling system, where a predominantly northerly wind regime in the summer months causes relatively cold, nutrient rich waters to be upwelled at the coast, thus enhancing the biological productivity of the region (e.g. Fiúza *et al.,* 1982). The relative importance of NIW mixing to primary production remains uncertain at the Atlantic Iberian margin, where upwelling is responsible for a large nutrient supply onto the shelf. It is likely that NIW mixing will further enhance the productivity of the region by promoting nutrient exchange across the thermocline.

An improved understanding of the relative importance of the NIWs to the biological productivity of the region would probably require a co-ordinated multidisciplinary approach, including further measurements of appropriate biological parameters and possibly the implementation of a coupled physical-biological model. Due to its dominant influence, internal mixing would have to be parameterized in any model of the Portuguese shelf in which the stratification was to be accurately represented.

Acknowledgments. The majority of this work constitutes part of the EU MAST II MORENA project (MAS2-CT93-0065). This is MORENA paper number 26. The remainder was funded by the EU MAST III OMEX II Phase I project (MAS3-CT96-0056). The captain and crew of the M/S *Håkon Mosby* are thanked for their cooperation with the field work.

REFERENCES

Apel, J. R. 1987. Principles of Ocean Physics. International Geophysics series, *38,* Academic Press, London, 634 pp.

Bogucki, D. and C. Garrett. 1993. A simple model for the shear-induced decay of an internal solitary wave. J. Phys. Oceanogr., *23,* 1767–1776.

Brickman, D. and J. W. Loder. 1993. Energetics of the internal tide on northern Georges Bank. J. Phys. Oceanogr., *23,* 409–424.

Fiúza, A. F. G., M. E. Macedo and M. R. Guerreiro. 1982. Climatological space and time variation of the Portuguese coastal upwelling. Oceanologica Acta, *5,* 31–40.

Haury, L. R., M. G. Briscoe and M. H. Orr. 1979. Tidally generated internal wave packets in Massachusetts Bay. Nature, *278,* 313–317.

Haury, L. R., P. H. Wiebe, M. H. Orr and M. G. Briscoe. 1983. Tidally generated high frequency internal wave packets and their effects on plankton in Massachusetts Bay. J. Mar. Res., *41,* 65–112.

Henyey, F. S. and A. Hoering. 1997. Energetics of borelike internal waves. J. Geophys. Res., *102*(C2), 3323–3330.

Holligan, P. M., R. D. Pingree and G. T. Mardell. 1985. Oceanic solitons, nutrient pulses and phytoplankton growth. Nature, *314,* 348–350.

Holloway, P. E. 1987. Internal hydraulic jumps and solitons at a shelf break region on the Australian North West Shelf. J. Geophys. Res., *92*(C5), 5405–5416.

—— 1991. On the dissipation of internal tides, *in* Tidal Hydrodynamics, B. B. Parker, ed., John Wiley and Sons, NY, 883 pp.

Howell, T. L. and W. S. Brown. 1985. Nonlinear internal waves on the California continental shelf. J. Geophys. Res., *90*(C4), 7256–7264.

Huthnance, J. M. 1989. Internal tides and waves near the continental shelf edge. Geophys. Astrophys. Fluid Dyn., *48,* 81–106.

Inall, M. E., T. P. Rippeth and T. J. Sherwin. 2000. The impact of non-linear waves on the dissipation of internal tidal energy at the shelf break. J. Geophys. Res., *105,* 8687–8705.

Jeans, D. R. G. and T. J. Sherwin. 2001. The variability of strongly non-linear solitary internal waves observed during an upwelling season on the Portuguese shelf. Cont. Shelf Res., (in press).

La Violette, P. E. and R. A. Arnone. 1988. A tide-generated internal waveform in the western approaches to the Strait of Gibraltar. J. Geophys. Res., *93*(C12), 15653–15667.

Lighthill, M. J. 1978. Waves in Fluids, Cambridge University Press, 504 pp.

Michallet, H. and E. Barthelemy. 1998. Experimental study of interfacial solitary waves. J. Fluid Mech., *366,* 159–177.

Miles, J. W. 1961. On the stability of heterogeneous shear flows. J. Fluid Mech., *10,* 496–508.

New, A. L. and R. D. Pingree. 1990. Large-amplitude internal soliton packets in the central Bay of Biscay. Deep-Sea Res., *37A,* 513–524.

Osborn, T. R. 1980. Estimates of the local rate of vertical diffusion from dissipation measurements. J. Phys. Oceanogr., *10,* 83–89.

Osborne, A. R. and T. L. Burch. 1980. Internal solitons in the Andaman Sea. Science, *208,* 451–460.

Pingree, R. D., G. T. Mardell and A. L. New. 1986. Propagation of internal tides from the upper slopes of the Bay of Biscay. Nature, *321,* 154–158.

Sandstrom, H. and J. A. Elliott. 1984. Internal tide and solitons on the Scotian Shelf: a nutrient pump at work. J. Geophys. Res., *89*(C4), 6415–6426.

Sandstrom, H., J. A. Elliott, and N. A. Cochrane. 1989. Observing groups of solitary internal waves and turbulence with BATFISH and echo-sounder. J. Phys. Oceanogr., *19,* 987–997.

Sandstrom, H. and N. S. Oakey. 1995. Dissipation in internal tides and solitary waves. J. Phys. Oceanogr., *25,* 604–614.

Sherwin, T. J. 1988. Analysis of an internal tide observed on the Malin Shelf, north of Ireland. J. Phys. Oceanogr., *18,* 1035–1050.

Simpson, J. H. and D. G. Bowers. 1984. The role of tidal stirring in controlling the seasonal heat cycle in shelf seas. Annales Geophysicae, *2,* 411–416.

Simpson, J. H., W. R. Crawford, T. P. Rippeth, A. R. Campbell and J. V. S. Cheok, 1996. The vertical structure of turbulent dissipation in shelf seas. J. Phys. Oceanogr., *26,* 1579–1590.

Thorpe, S. A. 1973. Experiments on instability and turbulence in a stratified shear flow. J. Fluid Mech., *61,* 731–751.

Received: *5 July, 2000;* revised: *7 March, 2001.*